Automated Design of a High-Power High-Frequency LCC Resonant Converter for Electrostatic Precipitators

T. B. Soeiro,
J. Mühlethaler,
J. Linnér,
P. Ranstad,
J. W. Kolar

Eidgenössische Technische Hochschule Zürich
Swiss Federal Institute of Technology Zurich

Automated Design of a High-Power High-Frequency LCC Resonant Converter for Electrostatic Precipitators

Thiago B. Soeiro, Jonas Mühlethaler, Jörgen Linnér,
Per Ranstad, *Member, IEEE*, and Johann W. Kolar, *Fellow, IEEE*

Abstract—This work presents an automated design procedure for series parallel resonant converters (LCC) employed in electrostatic precipitator (ESP) power supplies, which reduces the designer effort significantly. The requirements for the power supplies in ESP applications and means to derive an accurate mathematical model of the LCC converter, such as the power loss from commercial insulated-gate bipolar transistors, are described in detail in this paper. The converter parameters, such as resonant tank elements, are selected in order to improve the overall efficiency of the system, when a typical ESP energization operation range is considered. The analysis comprises two different control strategies: the conventional variable frequency control and the dual control. Both control strategies are analyzed by comparing semiconductor losses of five commercial modules. Finally, the circuit operation and design are verified with a 60 kW LCC resonant converter test setup.

Index Terms—Electrostatic precipitators, global optimization, LCC resonant converter.

I. INTRODUCTION

INDUSTRIAL electrostatic precipitators (ESPs) are reliable and robust air filters. They consist of parallel electrodes that use electrostatic charges to efficiently separate pollutant particles from a flowing gas, i.e., degrees of particle collection above 99% can be achieved [1]. When compared with fabric filters, their operating costs are low, and the risk of damage and stoppage owing to functional disorders is considerably smaller [2]. Power converters are used to supply energy to the ESP electrodes. These power supplies have a typical output power range of 10 kW to 120 kW and output dc voltage range of 30 kV to 100 kV [1]–[8].

Today, in many industrial sites, conventional mains frequency power supplies are still the most commonly used for ESP energization. Fig. 1 shows the basic circuit of such a conventional mains frequency high-voltage power supply, which are commonly referred to "transformer rectifier sets" (TR) [3].

As described in [1], the application of high-frequency power supplies for ESPs has significant advantages over the con-
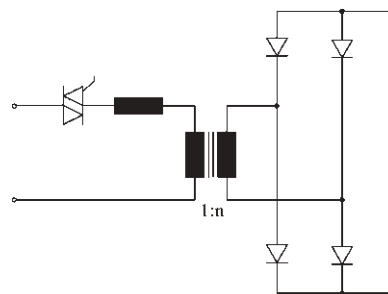
Fig. 1. Transformer rectifier sets.

ventional mains frequency energization. The high switching frequency operation allows for comparatively small overall size and low weight which simplifies the installation of equipment. More importantly, the high switching frequency also leads to a very smooth dc output voltage with negligible ripple and thus higher power in-feed to the precipitator which generally results in higher filtering efficiency. Another effect is the much faster control response that can be achieved. This leads to faster sparkover handling and also increases the efficiency, while reducing the stress on the ESP electrodes.

Fed by a three-phase mains connection, the high-frequency power supply behaves like a symmetric load. A power factor that is very close to unity and a better form factor of the input current over the whole operation range can be achieved, leading to reduced losses in the mains-side equipment [4]. The power conversion efficiency of the power supply itself is also significantly higher, and therefore the overall energy consumption can be reduced by using this converter technology instead of a conventional TR power supply [5].

For new plants, the application of high-frequency energization seems natural. In many cases, it can even make sense to consider an upgrade of already existing ESPs because the return on investment period is relatively short due to the higher efficiency that can be achieved [6]–[8].

High-frequency powered ESPs could be advantageously assembled with resonant converters, whose characteristics allow utilization of the parasitic elements of the high-frequency transformer into the circuit operation, while soft-switching for a wide operating range is preserved [2]–[17]. Fig. 2 shows the circuit of a suitable ESP power supply employing a series parallel resonant converter (LCC) with a capacitive output filter. The capacitor C_0 represents the electrical capacitance of the precipitator, which depends mainly on the geometric layout,
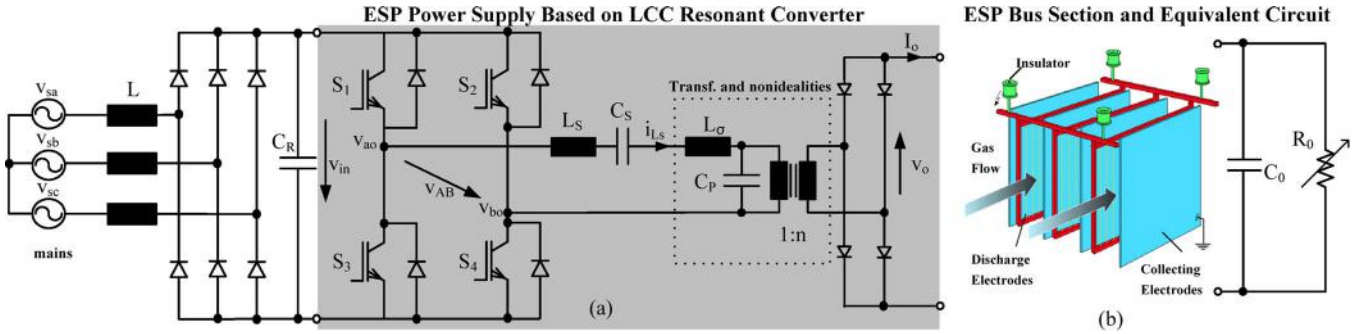
Fig. 2.   (a) Modern ESP power supplies based on LCC resonant converter; and (b) ESP bus section and equivalent circuit.

dimensions and, to some extent, on the dielectric properties of the processed gas [18]. The nonlinear resistance R_0 depends on the particle transport in the electrical field, and its value is inversely proportional to the particle loading [18].

The design of the LCC resonant converter shown in Fig. 2 is a very complex and time-consuming task as the operating characteristics of the system are strongly dependent on the load and the excitation frequency. In addition, due to the typically large parameter search space and the many project constraints for the ESP energization, the converter designer needs significant knowledge of the selected topology to manually refine the possible choices. Traditional designing methods for resonant converters are described in [17], [19]–[23].

The use of an accurate mathematical model describing the converter characteristics, i.e., the loss mechanisms of the system components, could remove the requirement for simulations. Additionally, the converter model allows the use of global optimization methods, such as the genetic algorithm (GA) [24], to simplify the design of the ESP power supply reducing the designer effort significantly, particularly during the initial phases.

In this paper, a GA is developed and presented to automate and accelerate the design of a 60 kW high-frequency power supply for ESPs based on LCC resonant converters. Requisites necessary for the optimal design of this system, resulting in high-power density and lower circuit component stresses, are described. The presented method reduces the design effort by identifying the characteristics of the candidate parameters of the converter with an accurate mathematical model of the LCC converter according to the type of soft-switching mechanism. A database with manufacturer information of suitable commercially available components is used in the designing steps to assess a prominent converter solution, giving to the designer a means of fine tuning the power supply performance.

In Section II, the characteristics of the power supplies of ESPs based on LCC resonant converters, including the features of two feasible control strategies, the conventional variable frequency (VF) control and the dual control (DC) [25], are shown. Section III presents the LCC converter analytical model and means to evaluate its performance regarding component losses for operation with VF or DC controls. In Section IV, a relatively simple design procedure for LCC resonant converters based on a set of rules, which are determined by the application requirements, is presented. The proposed ESP power supply design comprises both operation in pulsed mode and continuous energization with/without sparkovers. The structure of the

built GA optimizer is shown and its characteristics detailed. In Section V, the circuit operation and design are verified with a 60 kW LCC converter test setup, where both studied control strategies are compared by analyzing power losses of the insulated-gate bipolar transistor (IGBT) modules.

II. MODERN ESP POWER SUPPLY

A. High-Frequency ESP Power Supply

Due to the high dc voltage level requirements on the ESP, 30 kV to 100 kV, a transformer with a high turn ratio is commonly used to step up the voltage, and as a consequence, the secondary winding capacitance of the transformer is increased [6]. In addition, due to the isolation requirements, the windings of the transformer cannot be kept very close together, making the leakage inductance (L_σ) between the windings difficult to minimize. Fig. 2 shows a basic lumped element equivalent circuit of a high-voltage transformer.

In high-frequency ESP power supplies, the voltage to be fed to the high-voltage step-up transformer can be generated by a common pulse width modulation (PWM)-driven inverter or by a resonant converter. Experimental results of a hard-switching IGBT-based topology obtained by [1] showed significant deviations from the expected behavior, i.e., reduced efficiency, which was attributed to the influence of the parasitic components of the high-voltage transformer (L_σ and C_P). The incorporation of these transformer elements in their inherent resonant tank is, in contrast to the PWM inverter, one of the major advantages of resonant systems [10].

Resonant converters contain resonant L-C networks whose voltage and current waveforms vary sinusoidally during one or more subintervals of each switching period. The resonant network has the effect of filtering higher harmonic voltages such that a nearly sinusoidal current appears at the input of the resonant network [10]. This enables soft-switching of the IGBTs, which are most commonly used for mid-power converters, by placing the switching instant to current zero crossing (ZCS) or voltage zero crossing (ZVS). Thus, the switching losses are drastically reduced. The much lower switching losses, in turn, enable the use of much higher switching frequencies and thus a considerable reduction of the size of the passive components, such as the high-voltage transformer. Another benefit is the increase in power efficiency due to the lower losses when operating at moderate frequencies.
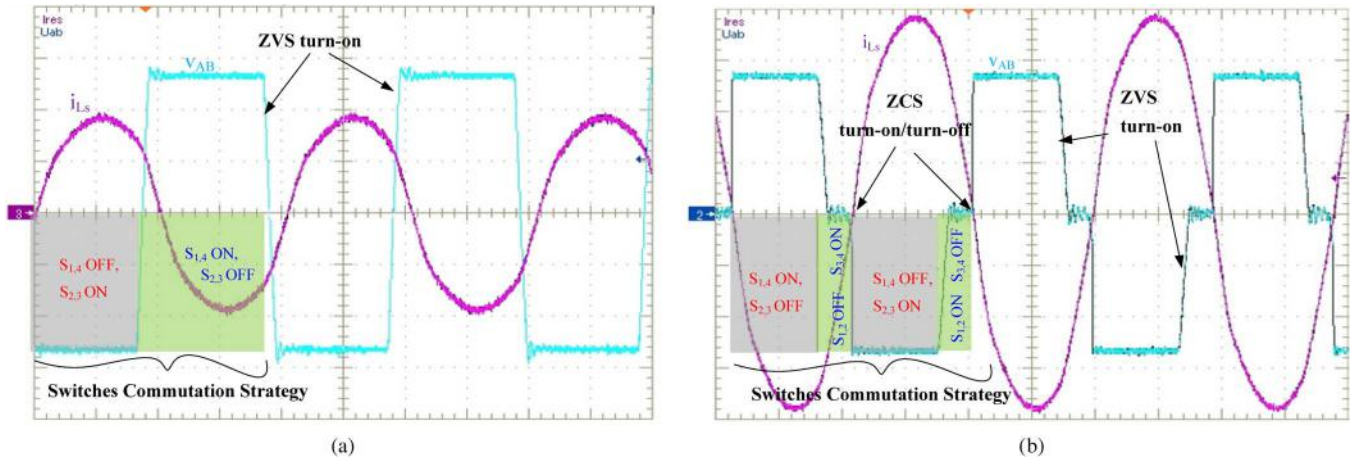
Fig. 3. LCC resonant converter experimental results: resonant current i_{Ls} (100 A/div; 10 μs/div) and inverter output voltage v_{AB} (200 V/div; 10 μs/div) for: (a) VF control, and (b) DC control. Note that, the signal i_{Ls} is inverted.

The LCC topology shown in Fig. 2 is particularly interesting for ESP applications as it can operate similarly to a series loaded resonant (SLR) converter for high load currents and to that of a parallel loaded resonant (PLR) converter for low load currents. Thus, one of the main drawbacks of the SLR, i.e., bad regulation behavior at low load current, can be solved because the LCC output voltage can be regulated at low load currents using a rather narrow frequency range (it behaves like a PLR) [10]. Also, one of the main drawbacks of the PLR, namely that for some combinations of C_P and C_S the resonant current shows only weak dependence on the load current, can be solved by the LCC converter. This combination of the characteristics of SLR and PLR can lead to better control behavior and also less sensitivity to component tolerances [7]. In addition, for the ESP operating range, the LCC topology has typically lower semiconductor losses and smaller peak (and *rms*) resonant current than the PLR converter [11]. This allows the choice of lower rated IGBTs and also smaller volume of the passive components. Finally, the switching frequency range needed to cover the typical ESP operation is smallest for the LCC converter.

The LCC converter can operate in three different modes with respect to the resonant, f_0, and switching frequencies, f_s: below resonance in discontinuous conduction (mode A: $f_s \leq 0.5f_0$); below resonance in continuous conduction (mode B: $0.5f_0 < f_s \leq f_0$); and above resonance (mode C: $f_s > f_0$). Two of them, mode A and mode C (with lossless snubbers), offer minimal switching losses. While, in fact, the semiconductor losses found in the discontinuous mode are typically the smallest due to the soft switching at turn-on and turn-off, this operating mode suffers from higher peak currents and also higher circulating energy within the resonant tank [12]. Moreover, a large frequency range is needed for the output voltage regulation which makes the design of inductive components difficult. Therefore, the operating mode above resonance is a feasible compromise between semiconductor losses and other characteristics such as stress of the passive components. Finally, these characteristics support the choice of an LCC topology operating above resonance for the final design of the 60 kW ESP power supply.

B. LCC Resonant Converter Control Strategies

The use of VF control is widespread for the LCC converter due to its simplicity and the even loss distribution between the full-bridge switches. The impedance of the resonant tank is controlled by changing the switching frequency of the full-bridge inverter. The switches in one leg maintain a 50% duty cycle, while the switches of the other leg are 180° phase shifted [cf. Fig. 3(a)]. This commutation scheme characterizes a two-level modulation of the inverter, where for operation above resonance, the four IGBTs commutate with ZVS. The switches turn on when the anti-parallel diodes are conducting (ZVS turn-on) and turn off with current. Therefore, losses are generated in the turn-off process, and lossless snubber capacitors are commonly employed. Another drawback of the VF control is that it normally requires a high switching frequency to reach low output current operation. Moreover, it suffers from high switching losses at high current and low output voltage operation [25]. The large frequency variation makes it difficult to optimize the magnetic components, gate circuitry, and the electromagnetic interference filters.

Alternatively, the output power of the LCC converter can be controlled by duty-cycle variation, where the operating switching frequency is automatically adjusted to ensure that the commutation of one bridge leg takes place at zero current (ZCS) and the other bridge leg at zero voltage (ZVS) [cf. Fig. 3(b)] [17] and [25]. This strategy, known as DC, incorporates characteristics of a phase-shift control and of a standard VF control. Consequently, the DC control narrows the switching frequency variation in relation to the handled power, overcoming the issue of high losses in the VF control during low output power operation. The feedback control diagram of the DC control is shown in Fig. 4.

One advantage of using the DC control strategy is the possibility of employing two different switch technologies. For example, one could utilize transistors with low conduction losses on the ZCS leg, and switches exhibiting low turn off loss on the ZVS leg. Although, the diodes D_2 and D_4 never conduct, in practice they have to be implemented. Due to the fact that the ZCS commutation cannot be triggered exactly at zero current and also because of the necessary dead-time
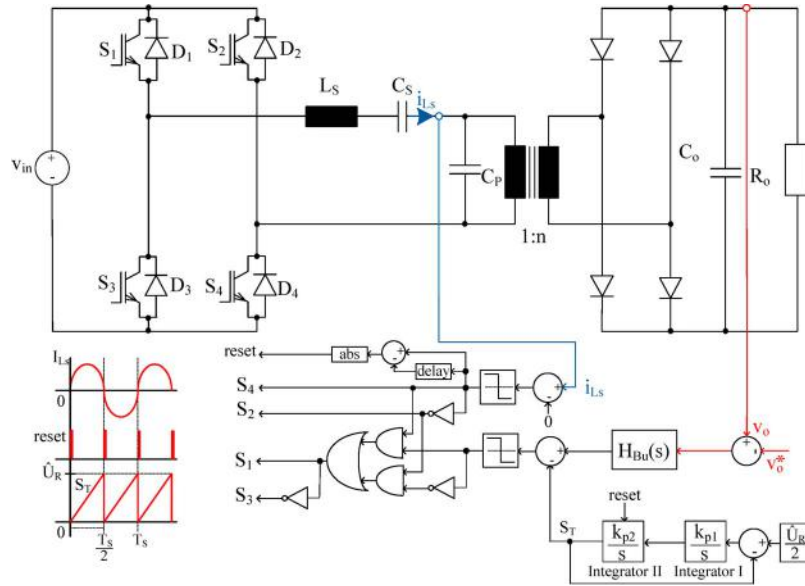
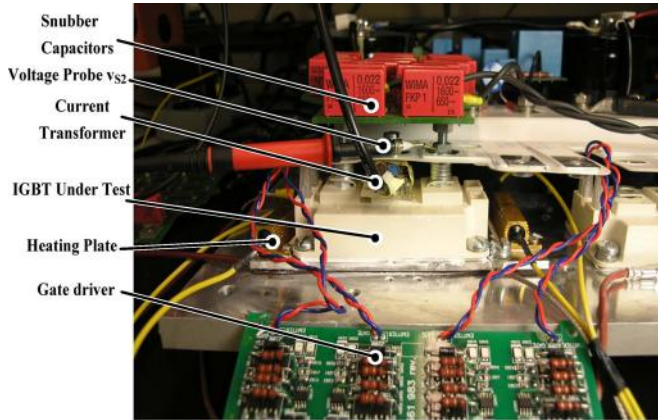Fig. 4.   Dual control basic diagram for LCC resonant converter.

Fig. 5.   60 kW LCC resonant prototype adapted to extract the switching loss characteristics of commercial IGBTs.

between both bridge-leg switches, D_2 and D_4 will conduct for a short time. A drawback of this strategy is the commonly uneven loss distribution between both legs of the full-bridge inverter which makes the designing of a compact cooling system more complex. This is due to the fact that the ZCS switches are conducting current almost 50% of the switching period, while the turn-on interval of the ZVS switches is dependent on the duty cycle [15].

Fig. 3(a) and (b) show the main waveforms of a 60 kW water-cooled LCC resonant prototype (cf. Fig. 5) operating with VF and DC controls, respectively. In these analyses, the converter is fed by a 540 V dc-link voltage.

C. ESP Typical Operation Modes

As shown in Fig. 6, industrial ESPs are normally divided into several bus sections in order to increase the particle collection efficiency [2]–[5], and [18]. These sections have different electrical behavior and efficiency, due to: different dust loads; particle size and properties; and the possibility of charging particles using appropriate technology, i.e., pulsed or continuous energization [18]. Therefore, these bus sections are

normally energized by dedicated power supplies with different power levels fed by the same grid.

The continuous energization is usually applied where the particle concentration is very high (inlet fields). In order to achieve optimal precipitation efficiency, a high power supply (>50 kW) operating at a dc voltage level very close to the sparkover limit is commonly used. Frequent sparkovers may occur in this operating mode, and a de-ionization time is necessary to prevent repetitive sparks [3]. A sparkover is a breakdown of the flowing gas dielectric of the ESP, which short-circuits the ESP electrodes.

In pulsed operation, the ESP is fed with periodic high-voltage pulses, which improves the collection efficiency of high resistivity dusts (middle and outlet fields) and reduces energy consumption [3]. The circuit presented in Fig. 2 is suitable for both energization techniques, but adaptation of the output control reference signal is needed. In order to collect fine particles more efficiently, the output reference signal of a pulsed power supply is normally adjusted to be higher than one which would operate in continuous mode.

III. LCC CONVERTER: LOSS PREDICTION MODEL

In this section, the LCC converter analytical model and means to evaluate its performance regarding component losses for operation with VF or DC controls are presented.

A. Semiconductors Loss Prediction Model

Based on the modified first harmonic analysis proposed in [20], the equations describing the LCC converter behavior are derived for VF and DC control strategies [cf. (1)–(12)]. The stress on all converter power components can be calculated by (13)–(25). The expressions of electrical current through the semiconductors as a function of the operating point, given by the phase displacement ϕ between the first harmonic of the inverter output voltage, and the resonant current and/or the inverter duty cycle D, can be combined with the loss characteristics of commercially available IGBTs, in order to accurately
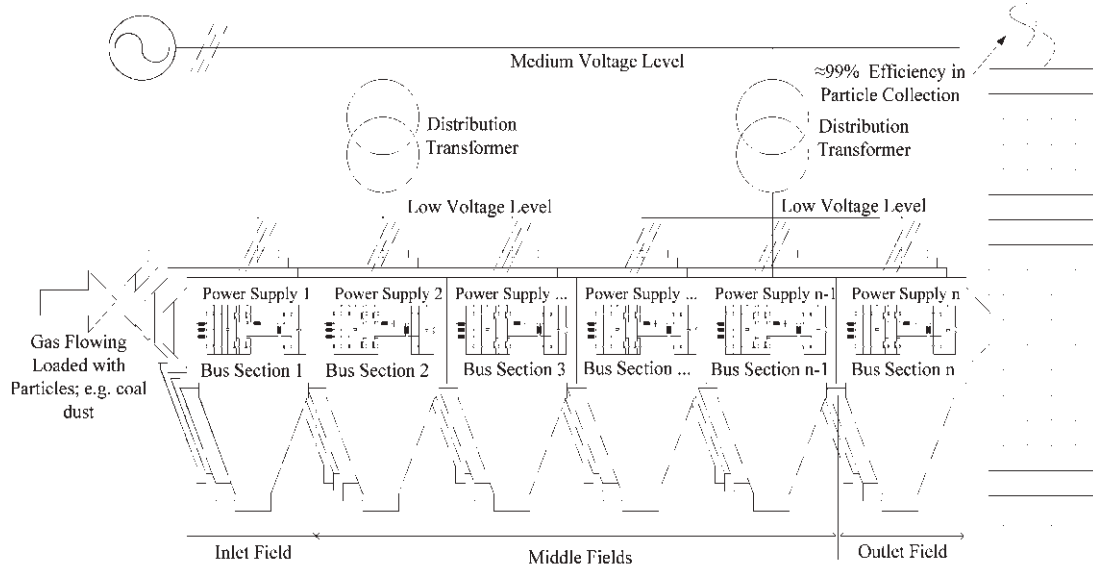
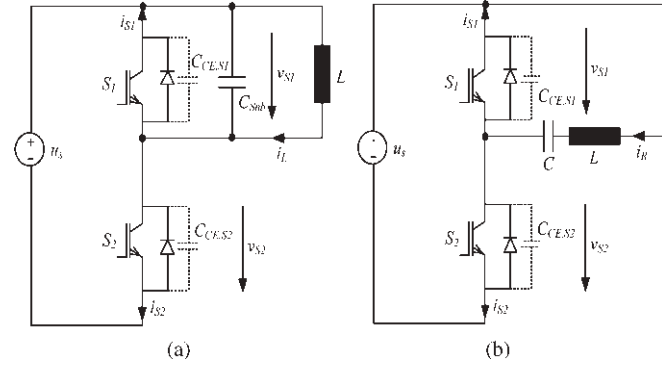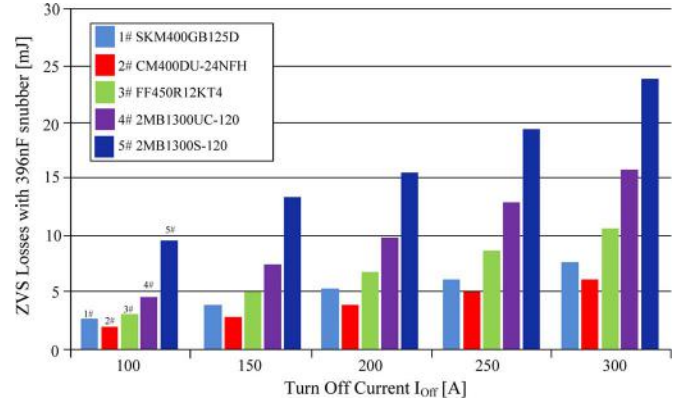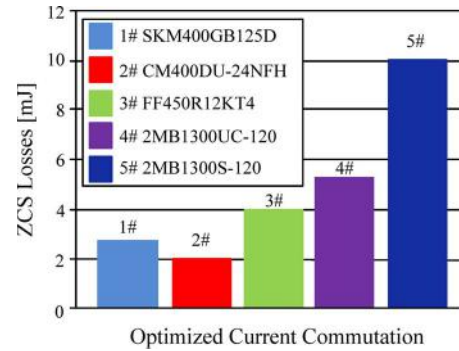Fig. 6.   Typical ESP installation scheme of a system with 24 power supplies.

(a)   (b)

Fig. 7.   Test circuits for (a) ZVS and (b) ZCS switching loss characteristics.

Fig. 8.   ZVS turn off measurement results, $T_J = 125\,°C$ and $C_{Snb} = 396$ nF.

Fig. 9.   ZCS losses, $T_J = 125°C$ and $t_d =$ optimal.

predict the total semiconductor losses for a converter with a specific arrangement of components. In this way, the loss prediction model is built and used in an optimization strategy, in order to design the LCC converter for minimal component losses.

Equations (26)–(31) describe the semiconductor losses for VF control, where u_S represents the dc-link voltage used to extract the loss model (cf. Fig. 7). For DC control, the semiconductor power losses are given by (32)–(37), where E_{optm} is the optimal switching energy for the ZCS bridge leg [2]. With the semiconductor losses dissipated via a heat sink, the maximal allowed thermal resistance of the heat sink $R_{th,S-A}$ could be calculated by combining the total power loss calculated with the desired maximal heat sink temperature T_{Sink} and environmental temperature T_{Amb} as given by (38).

The semiconductor power loss model is obtained according to [26]. The loss model is described with dependency on the instantaneous current I_C through the semiconductor and the turn-off current I_{C_off} as shown in (26) and (27). a_i, b_i, and c_i are the second-order equation fitting coefficients obtained by datasheet and/or experimental analysis. Due to their low turn-off energy and conduction loss characteristics, five commercially available power modules were selected as candidates for use in the 60 kW prototype. The switching loss characteristics of these power modules for ZVS and ZCS switching are obtained directly in the 60 kW LCC prototype shown in Fig. 5,

where the test circuits shown in Fig. 7 were assembled. In this paper, the second-order fitting coefficients for conduction losses of IGBTs and diodes as a function of the junction temperature, T_j, were obtained directly from the datasheets.

In Fig. 8, the results for ZVS of all analyzed semiconductors are summarized in a bar chart for $T_j = 125°C$ and $C_{Snb} = 396$ nF. For ZCS, the results of all analyzed IGBTs are summarized in the bar chart of Fig. 9 for optimal dead time, t_d.

For the output rectifier diodes, an approximately constant forward voltage drop $V_{F,R}$ is assumed so that the conduction losses $P_{C,R}$ in each diode can be calculated with the average
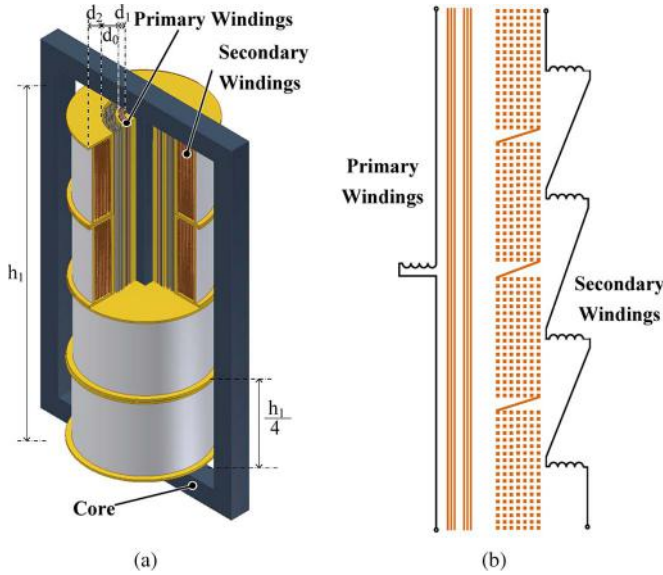
Fig. 10. Oil-immersed high-voltage transformer for high-frequency high-power applications [cf. [28]]: (a) structural schematic of the transformer; and (b) windings connection details.

current by (39). As this rectifier is built by series connection of high-voltage fast diodes, the switching loss is relatively small and, thus, is neglected. Due to insulation and cooling matters, the high-voltage rectifier can be contained together with the transformer in an oil-filled vessel.

B. Resonant Capacitors Power Loss Model

In resonant converters, the series and parallel capacitors are subject to high-power loss due to the flowing current and voltage with high amplitude and frequency. In order to limit the losses and the temperature rise, dielectrics with low loss factor $(tan\delta)$ are required.

The power loss in capacitors is generally caused by two phenomena: dielectric losses and thermal losses. The former is caused by the cycle of charging and discharging of dielectrics, while the latter is due to the currents flowing through the electrodes. The dielectric losses P_d as well as the thermal losses P_{tm} can be determined by (42) and (43), respectively. Metalized film capacitors from High Energy Corp. are considered in the design.

C. High-Frequency Transformer and Series Inductance

A high-voltage, high-power transformer suitable for ESP applications is shown in Fig. 10 [28]. The construction details are shown in Fig. 11.

Sufficient distance between the primary and the secondary windings (d_0) has to be provided in order to obtain effective insulation voltage. Oil could be selected as the main insulation material as improved heat dissipation, stronger insulation characteristics, and lower insulation permittivity can be achieved when compared with air at normal atmospheric pressure [27]. In order to avoid bridge breakdown phenomena, the use of wave boards between the primary and secondary windings and also between the secondary windings and the transformer tank are recommended [28]. Additionally, each layer of the primary and
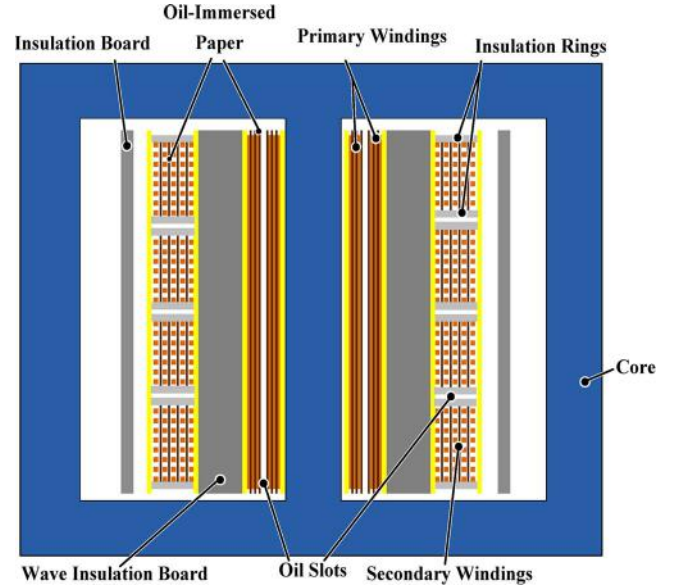

Fig. 11. Structural schematic of a high-frequency high-power transformer [28].

secondary windings can be insulated from one another with oil-immersed paper.

For the transformer shown in Fig. 10, the equivalent leakage inductance can be modeled as the lumped series inductance L_σ as shown in Fig. 2, and its value can be calculated by (40) [29]. In the case where the distributed winding capacitances are treated as a lumped parallel capacitance C_P referred to the primary side of the transformer (cf. Fig. 2) its value can be determined by (41) [30]. Therefore, by adjusting the transformer dimensions one can optimally design these elements in order to incorporate them into the LCC resonant converter operation. However, a tradeoff between the desired parasitic values and the insulation distance should be considered.

As in [27], the magnetic and thermal design considered in this work is based on the McLyman method [29]. However, the core and copper losses are calculated differently. The core loss, which is a result of hysteresis, eddy current, and stray losses, is calculated by the approach presented by [31], based on the Steinmetz law along with the voltage waveforms. The copper losses are calculated including skin and proximity effect loss by a 1-D approach as for the example presented in [32]–[34] [cf. (44)–(47)]. Due to the approximately sinusoidal current in the primary winding, only the fundamental harmonic can be considered in the loss and optimal foil thickness calculation.

IV. LCC CONVERTER: DESIGN PROCEDURE

In this section, an automated design procedure for LCC resonant converters based on a set of rules, which are determined by the application requirements, is presented (cf. Fig. 12). A bandwidth-limited design methodology is used, where the converter's performance with a set of parameters is evaluated, regarding its main component losses, in a specified operation range. The design comprises both the ESP operation modes and the control strategy used for the LCC converter (VF or DC controls). A GA is developed and used to accelerate the solution convergence to the set of parameters $(C_P, \alpha = C_P/C_S, f_s, \text{ and } n)$ which optimally design the ESP's LCC resonant converter regarding power density and low circuit component stresses, while
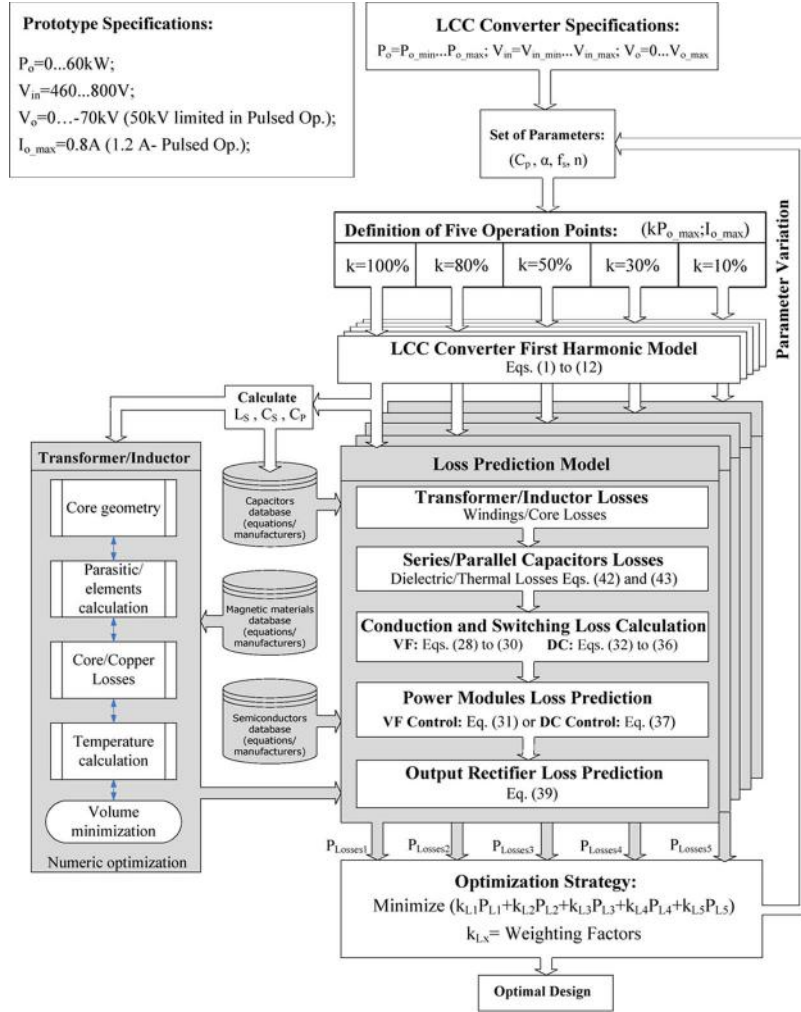
Fig. 12. LCC converter design strategy flowchart. Equations (1) to (48) are presented in the Appendix.

many design constraints are fulfilled. Note that a "brute-force" approach or another global optimization strategy (GOS) could be used to the same end. In the first, all possible solutions should be evaluated always ensuring the track of the best set of parameters for the problem at hand. However, compared to GOSs, the computational time of the "brute-force" strategy is much higher. Among the global optimization strategies, the GA is very robust, easily programmed, and provides a relatively fast convergence. These are the reasons this strategy is studied further.

A. LCC Resonant Converter Design Procedure

The sum of the power losses of the LCC converter components for five operating points are predicted for a set of circuit parameters (C_P, α, f_s, and n) by analyzing the mathematical model of the LCC resonant converter (cf. [20]) and the component's characteristics obtained from experimental analysis and/or datasheet values. The optimal set of parameters is determined by tracking the arrangement which results in minimal circuit component stresses, when the input voltage of the converter and power capability are defined.

From the first harmonic analysis of the system operating behavior, one obtains for a defined control strategy (VF or DC control), output voltage V_0 and output current I_0, the set of

(1) to (12). These equations are condensed into a nonlinear equation $V_0 = f(V_0, I_0, f_{sN})$. This is then used to numerically determine a unique $f_{sN} = f_s/f_o$, by combining the set of parameters (C_P, α, f_s, n), with the specified operation condition for maximum loading P_{0max} and minimum input voltage V_{in_min}. The necessary resonant circuit elements, L_S and C_S, to fulfill this operation are then calculated. In the next step, an inner loop optimizes the geometry of the high-voltage transformer and series inductor while keeping the temperature below the allowed limits. Similar magnetic design approach is shown in [27], where the McLyman method is used. The series capacitor C_s can be selected by using a database which stores characteristics of commercial components.

With the LCC converter components designed and for a specific operation point given by V_{in}, V_0, and I_0, a unique f_{sN}, ϕ, D, and f_s can always be found. Hence, the converter power loss performance for an operation range can be predicted by evaluating the stress on all power components [cf. (13)–(47)].

A function which adds up the component power losses obtained for the set of parameters (C_P, α, f_s, n) in five operation points is used to assign a value to this designed LCC converter. This function is minimized by an optimization strategy based on GAs. In fact, the GA is used to accelerate the solution convergence by selecting sets of parameters which have the best

chances of fulfilling the problem goal. Weighting factors can be utilized to give the analyzed operation points different degrees of importance and also to give a penalty gain in cases where some requirements are not fulfilled.

A flowchart describing the design optimization strategy and the 60 kW prototype specifications is shown in Fig. 12. The restriction or requirements for this application are translated as optimization constraints, which are described as follows.

- Switching frequency f_s is limited to $f_{smax} > f_s > f_{smin}$. The bottom limit f_{smin}, which can be reached mainly in pulsed mode, is selected in order to avoid operation in the audible noise spectrum and to minimize volume of passive elements. The upper limit f_{smax} is determined by the power semiconductor switching loss, gate drive, and signal electronics delay times on the operating behavior. The maximal switching frequency can be reached at high input voltage and/or low power operation (i.e., during sparkovers).

- The maximum voltage stress on the series capacitor C_S has to take into consideration the range of capacitor technology available for high-frequency and high-current applications.

- The capacitance of the parallel resonant capacitor C_P has to take into consideration the minimum achievable winding capacitance of the high transformer employed in the case at hand. The upper limit is determined by the converter operating range, which is strongly dependent on $\alpha = C_P/C_S$ [17]. For lower values of α, the frequency range will be wider than for higher values. Note that, as shown in (41), the parallel capacitance (C_P) is a geometrically dependent parameter, and a desired value can be obtained by optimally designing the transformer dimensions.

- The series inductance L_S can be set to be smaller than the maximal achievable leakage inductance (L_σ) of the transformer [cf. (40)]. If this condition is not satisfied, a penalty can be added to the GA fitness function. On the other hand, the total series inductance ($L_S + L_\sigma$) and the series capacitance C_S are the components which limit the short-circuit current peak across the semiconductors during sparkovers. In this way, for the bottom operation frequency f_{smin} (at maximum power), the current peak I_{Lspk} during sparks should be determined, and its value should be limited according to the maximum collector current I_{CM} of the IGBT and the rate current of the anti-parallel diode I_{FM} ($I_{Lspk} < I_{CM}$ and $I_{Lspk} < I_{FM}$).

- The minimum transformer turns ratio n is determined according to the minimal input, V_{in_min}, and maximal output voltages at full power. If a small n value is used, a lower current would flow in the main circuit, thereby lowering the losses. However, this could mean that the system operates at switching frequencies close to resonance f_o. To preserve the desired soft-switching characteristic, the normalized frequency must fulfil $f_{sN} = f_s/f_o > 1.1$[35]. Note that, for the power supply shown in Fig. 2, V_{in_min} has to consider not only the minimal allowed voltage operation of the grid, but also the drop of the dc link voltage which is expected in pulsed operation (cf. Fig. 19).
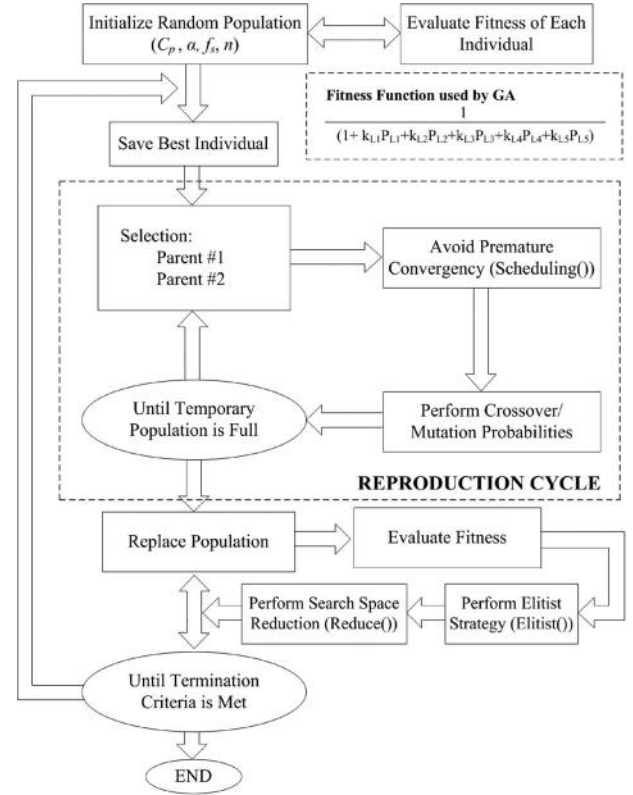

Fig. 13. Complete structure of the built GA. Refer to [24] and [36]–[39].

- The error between the design specification point and candidate point is used to add a penalty to the optimized function, e.g., if V_o cannot be reached (cf. (48)).

B. Optimization Strategy Based on GAs

A flowchart showing the complete structure of the developed GA optimizer is presented in Fig. 13.

During the GA optimization, a set of trial solutions, or individuals, is chosen, and for each one, a fitness value is assigned by evaluating the fitness function built following the flowchart illustrated in Fig. 12. For the LCC converter design, each individual is represented by a set of parameters that are regarded like the genes of a chromosome (C_P, α, f_s, n) [24].

In each cycle of genetic operation, a subsequent generation (offspring) is created from the chromosomes in the current population (parent). The genes of the parents are mixed and recombined for the production of offspring in the next generation. An operation rate (p_{cross}) is used as the probability of crossover. In order to facilitate the GA evolution cycle, a mutation function is used to perturb the mated population [36]. It is expected that from this process of evolution (manipulation of genes), the "better" chromosome will create a larger number of offspring, and thus has a higher chance of surviving in the subsequent generation (most likely to be the best solution), emulating the survival-of-the-fittest mechanism in nature [36]. Fitness values are evaluated for, and assigned to, each of the new individuals by following Fig. 12. The termination criterion is then evaluated, which can be for example a predefined number of iterations.

The functions Scheduling(), Elitist(), and Reduce() can be used to improve the convergence of the GA. For more details in GA theory, [24] and [36]–[39] are recommended.

C. Optimization Example

In this section, an example showing how the optimization evolves following the flowcharts illustrated in Figs. 12 and 13 is given. The analysis considers the VF control and IGBT#3.

In a first step, the GA initializes a predefined number of random trial solutions, e.g., $nvar = 100$, within the range of C_P, α, f_s, and n established by the user. For example, the trial solution ($C_P = 120$ nF, $\alpha = 0.086$, $f_s = 23.5$ kHz, $n = 152$) which is found in the range ($C_P = 0.1 \ldots 1.5$ μF, $\alpha = 0.02 \ldots 1$, $f_s = 22 \ldots 30$ kHz, $n = 152 \ldots 200$). Note that the space solution must satisfy the optimization constraints listed in Section IV-A.

In the next step, for maximum loading $P_{0max} = 60$ kW and minimum input voltage $V_{in\_min} = 460$ V, each solution has its resonant tank elements assigned according to (1)–(12). These equations are condensed into a nonlinear equation $V_0 = f(V_0, I_0, f_{sN})$, which is used then to numerically determine a unique $f_{sN} = f_s/f_o$. The values of C_S and L_S are selected from α and f_o (from $f_{s,N}$). For the example at hand, $f_{s,N} \approx 1.13$, which gives $C_S = 1.4$ μF and $L_S = 42$ μH. In case the restriction $f_{s,N} > 1.1$ is not satisfied, the solution is rejected and replaced by another trial solution assigned by the GA.

In the next step, the high-voltage transformer and series inductor are designed. For each set (C_P, α, f_s, n), a "brute-force" optimization takes place, and the magnetic device solutions with minimal volume are selected. For the considered example ($C_P = 120$ nF, $\alpha = 0.086$, $f_s = 23.5$ kHz, $n = 152$), many transformer solutions are derived as shown in Fig. 14. Note that the losses and geometry of the transformer are calculated from (44)–(47) and Fig. 10. The insulation distance, filled with oil-immersed paper, between the primary winding and the core, and also between the primary/secondary winding layers is set to 1 mm, which gives an operating field strength of up to 40 kV/mm. Additionally, the insulation distance between the high-voltage winding and the other components (core, primary, case) is set to be 4 cm, which includes a relatively large safety margin as a breakdown field strength of about 6 kV/mm can be used for transformer oil [27]. The transformer parasitic elements, L_σ and C_W, are determined by (40)–(41) and they are considered in the design of L_S and C_P. Finally, the values of C_S and C_P are compared and selected from the list stored in the database.

The converter power loss performance for the five specified operation points can be predicted by evaluating the stress on all power components [cf. (13)–(47)]. In the next step, the converter power loss is evaluated for nominal input voltage. Therefore, the fitness function for both input voltage operation conditions are added and used as a measure of the solution performance. The set of parameters achieving the best performance from all trial solutions is stored. Note that in case that V_o cannot be reached in any of the five operation points, a penalty is added to the optimized function as given in (48). For the example at hand, for full power and minimal input voltage, the total semiconductor loss is about 550 W. For full power and nominal input voltage (540 V), the total semiconductor loss is about 795 W.

It is important to point out that a function $Roulette()$ is used to select stochastically two sets of parameters to perform crossover. Here, the probability of selecting a specific solution from the total list is proportional to its relative fitness. There-
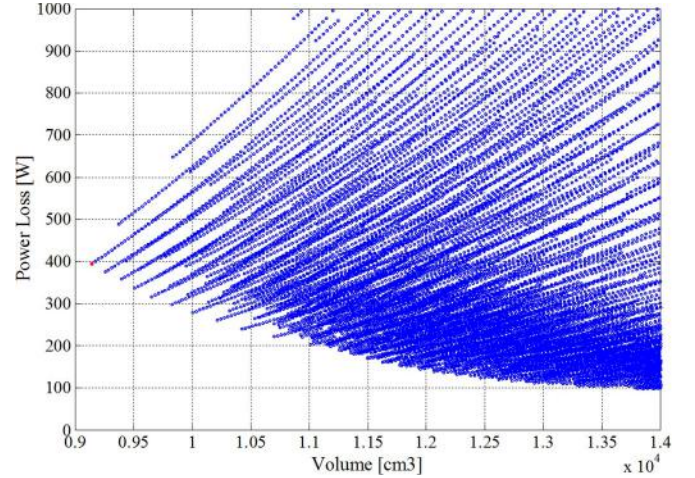

Fig. 14. Many suitable transformer designs for ($C_P = 120$ nF, $\alpha = 0.086$, $f_s = 23.5$ kHz, $n = 152$). The selected design with the lowest volume is shown.

fore, solutions with high fitness will participate in the creation of the next generation more often than less-fit ones. In order to avoid a premature convergence of the GA, that is, the solution search being confined in a local solution space, the number of times a specific set of parameter can be selected to perform crossover is limited ($Scheduling()$).

The parameters of the selected pair ($C_{P1}, \alpha_1, f_{s1}, n_1$) and ($C_{P2}, \alpha_2, f_{s2}, n_2$) are mixed in order to generate other $nvar$ numbers of solutions. The crossover objective is to produce a better combination of parameters, hence resulting in fitter solutions. This process occurs according to a probability operator p_{cross}, e.g., $p_{cross} = 0.6$–0.9. For each parameter, if the random pointer p, in the range $0 \leq p \leq 1$, is $p > p_{cross}$, the parameter of each pair is copied into the two new set of parameters. On the other hand, if $p \leq p_{cross}$, a mating process takes place. Here, random multiplier coefficients β_1 and β_2, in the range $0 \leq \beta \leq 1$, is used to combine the current parent parameter in order to create the new offspring. For example:

- $C_{P\_offspring1} = \beta_1 C_{P1} + (1 - \beta_1)C_{P2}$;
- $C_{P\_offspring2} = \beta_2 C_{P2} + (1 - \beta_2)C_{P1}$.

A mutation operator is used to explore portions of the solution space that are not represented in the current set of parameters (population). For each solution, if the random pointer p, in the range $0 \leq p \leq 1$, is $p \leq p_{mut}$, a parameter (C_P, α, f_s, or n) is randomly selected and changed. A coefficient $k_{mut} = (1 + 0.05\beta)$, with $-1 \leq \beta \leq 1$, is multiplied to the selected parameter. If $p > p_{mut}$, the parameter is kept without modifications. Herein, the mutation occurs with a low probability, $p_{mut} \leq 0.1$. Note that after $crossover()$ and $mutation()$, the parameters should always respect their range defined by the user, e.g., ($C_P = 0.1 \ldots 1.5$ μF, $\alpha = 0.02 \ldots 1$, $f_s = 22 \ldots 30$ kHz, $n = 152 \ldots 200$).

For each new solution, the flowchart of Fig. 12 is used to evaluate its fitness. In the end of each cycle, the best solution is saved and a new reproduction cycle begins. This process occurs until a number of cycles, n_{cycle}, have been performed.

Due to the probabilistic nature of the GA selection, crossover and mutation, it could happen that for the current set of solutions, the best set of parameter has lower fitness than a preceding generation. If this is observed, some of the best set
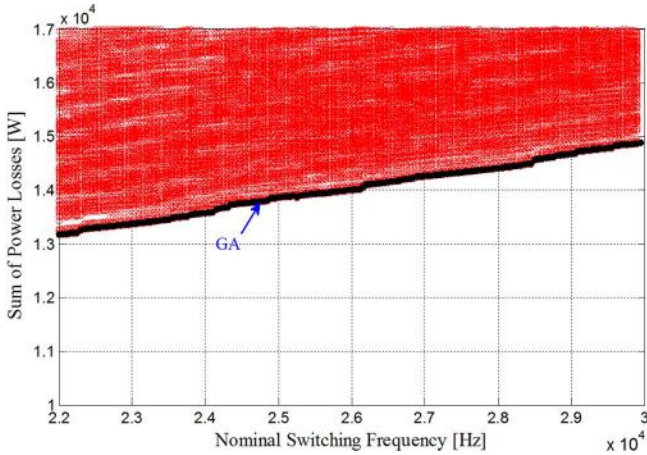
Fig. 15. Sum of converter power losses for minimal and nominal input voltages at five specified loading points as function of the nominal switching frequency for many suitable LCC resonant converter designs obtained with the built GA and "brute-force" optimizers. The bottom line represents the optimal result obtained with the GA optimizer while all the other results are from the "brute-force" strategy.

of parameters from the preceding solutions are inserted into the new generation ($Elitist()$). Additionally, in order to accelerate the solution convergence, as the number of reproduction cycles reaches 90% of n_{cycle}, a function $Reduce()$ selects the best solution of the current list and from that new set of solutions are generated by performing random disturbances in its parameters, e.g., perform $mutation()$ with high probability $p_{mut} = 0.85$. For the last 10% reproduction cycles, 20% of the new generation is selected in this way.

Finally, when the total number of cycles is reached, the user can select one of the set of parameters from the list of the best achieved solutions.

Fig. 15 shows the performance achieved with the built GA optimizer when tracking the set of parameter which gives the minimum total circuit losses as function of the nominal switching frequency defined by the nominal operating condition ($P_0 = 60$ kW and $V_{in} = 540$ V). In order to ease the reader understanding, instead of the fitness function given in Fig. 13, the performance shown for each suitable LCC design is the indicator of total converter power loss given as the sum of the power loss calculated at the five specified loading operations for both defined input voltages of the converter (minimal and nominal values). Note that the result obtained with a "brute-force" optimization is also shown. Therein, it can be seen that the proposed automated design strategy worked satisfactorily as the GA optimizer could rapidly identify, for each analyzed switching frequency, a best solution with performance very close to the one obtained with the "brute-force" strategy. In this investigation, the computational time used by the GA optimizer was around 20 times faster than the one used by the "brute-force" strategy. This time difference is not only defined by the GA termination criteria and the number of GA trial solutions, but also by the desired accuracy of the "brute-force" strategy that determines the total number of possible set of parameters (in the case at hand was 2 millions). For the GA optimizer, the termination criterion was a number of iteration equal to 500 while the number of random trial solutions was set to 100.
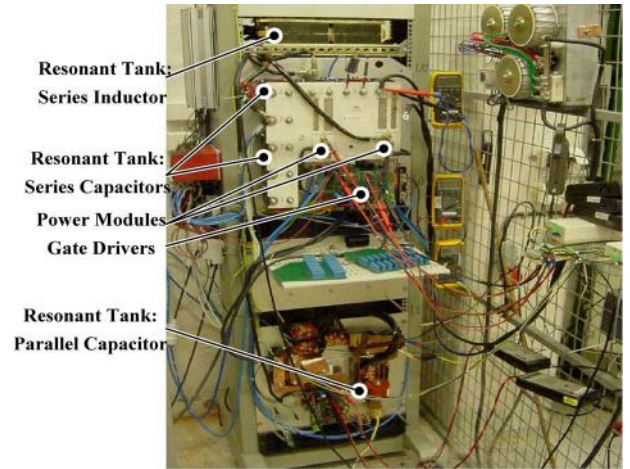

Fig. 16. Test setup.
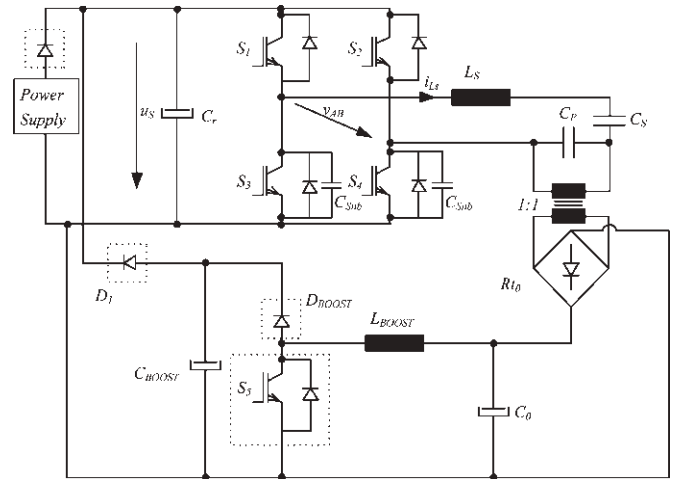
Fig. 17. Test setup circuit diagram.

V. EXPERIMENTAL VERIFICATION

In order to determine the most suitable IGBT power module and control strategy for the LCC resonant converter specified project, first the constructed GA optimizer was used to obtain a set of optimized parameters (C_P, α, f_s, n), and to predict losses for both VF and DC controls. To validate the calculations, the losses for the power IGBT modules are evaluated in an assembled 60 kW test setup converter. The experimental system and the circuit diagram are shown in Figs. 16 and 17. Therein, the transformer with high turns ratio was replaced by a 1 : 1 transformer. This system consists of a LCC resonant and a regenerative boost converter, where the latter acts as an electronic load and also feeds the output power back to the dc link of the main converter. In this way, the power supply is used only to compensate the system losses. The IGBT losses are measured calorimetrically, by measuring the rise in temperature of the cooling water, which is circulated at a constant flow rate. The resonant components were selected to be the same for all control strategies and power semiconductors, as a compromise between all the GA optimal results. Thus, for a specific operation point and control, each analyzed module commutates at similar switching frequency, giving similar stress to the other circuit elements. Fig. 3 shows the resonant current i_{Ls} and the

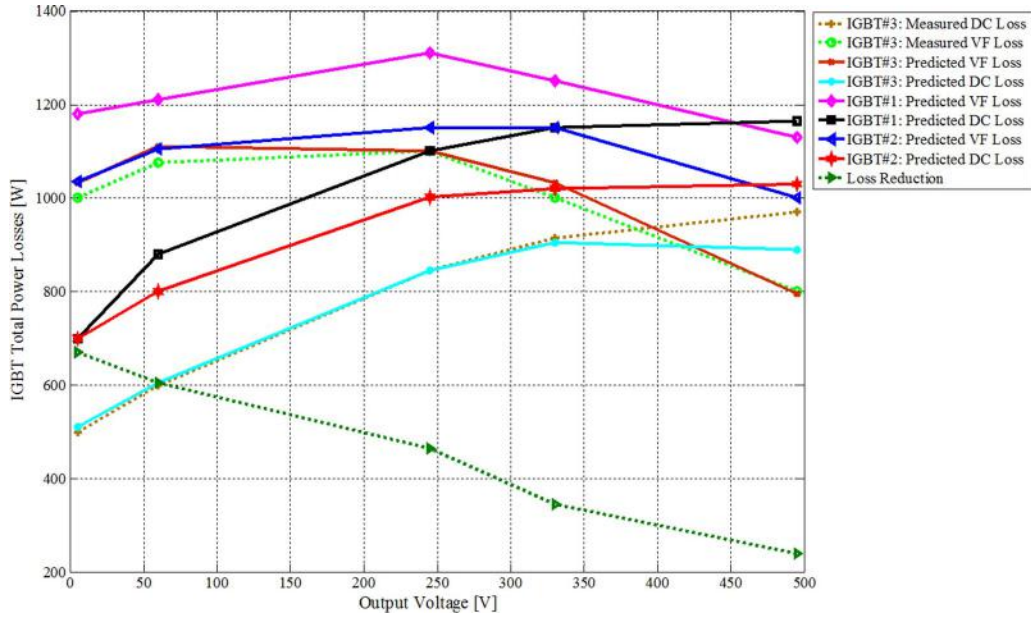Fig. 18. Power loss model verification and loss results. Here, $V_{in} = 540$ V.

inverter's output voltage obtained experimentally for VF and DC controls.

For the sake of brevity, the loss model verification (experimental results/model prediction) is shown in Fig. 18 only for the IGBT #3 (FF450R12KT4); however, the same accuracy ($\pm 5\%$) is obtained for the other IGBTs. Fig. 18 also presents the comparative results for three of the power modules tested and the control strategies studied. The analyses are made in continuous operation mode at a constant current of 120 A and for different output voltages, 0 to 485 V. A graph comparing the results for the semiconductor that obtained the highest losses against that with the lowest loss results in the considered voltage range is shown in Fig. 18. As one can observe, the power loss reduction can range from 230 W to 660 W, for maximum and minimum analyzed output voltages, respectively.

Note that, from the design point of view, each system needs to consider the operation point with highest losses. By analyzing Fig. 18, it can be observed that for VF control, this operation condition is located in between the operation points of $20\%V_{o\_max}$ and $40\%V_{o\_max}$, while for DC control, it is located above the operation point $70\%V_{o\_max}$. For all analyzed power modules, the difference between the maximum semiconductor losses for DC control against VF control is in the range of 150 W. Therefore, for all designed converter, the ones employing DC control requires smaller cooling systems.

In Figs. 19 and 20, the typical waveforms of an ESP power supply based on diode bridge rectifier (front-end) and a LCC resonant converter (back-end) when operating in pulsed mode are shown. The pulse mode operation is selected for evaluation because important aspects of the ESP energization discussed in Section II-C can be seen. To perform the tests, a high-voltage R-C load emulating the ESP was utilized to withstand an applied pulsed voltage V_{ESP} from 0 to -62 kV with pulse repetition of 24 ms. Therein, the pulse is released only during

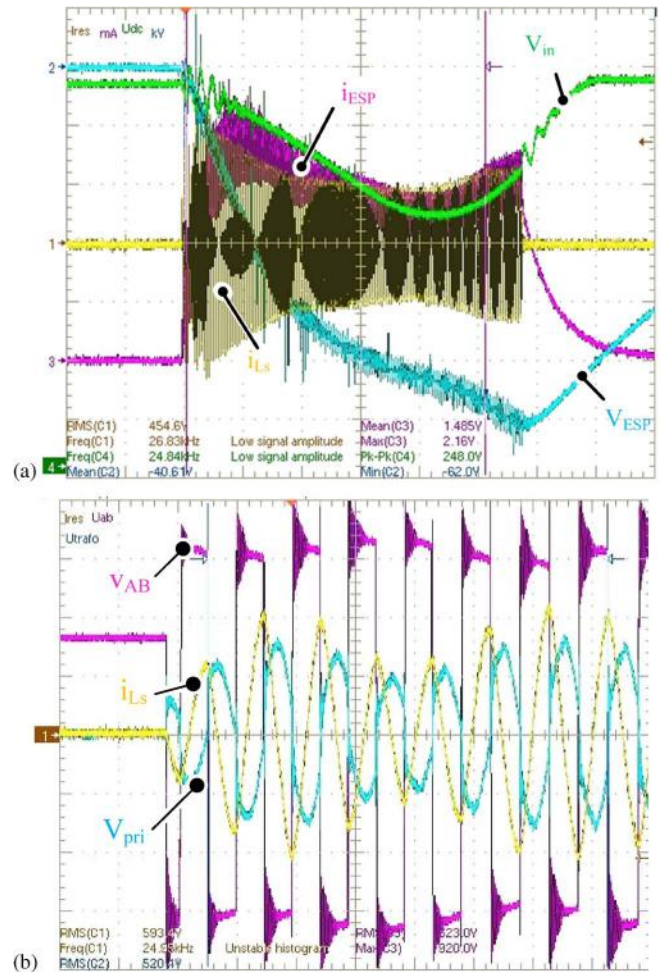Fig. 19. Pulsed operation main waveforms. (a) Resonant tank current i_{Ls} (100 A/div); output voltage V_{ESP} or V_0 (10 kV/div); current i_{ESP} or i_0 (250 mA/div); and bus-bar voltage V_{in} (100 V/div). (b) Resonant tank current i_{Ls} (100 A/div); full-bridge output voltage V_{AB} (200 V/div); and transformer primary voltage V_{pri} (500 V/div). Signal V_{pri} is inverted.
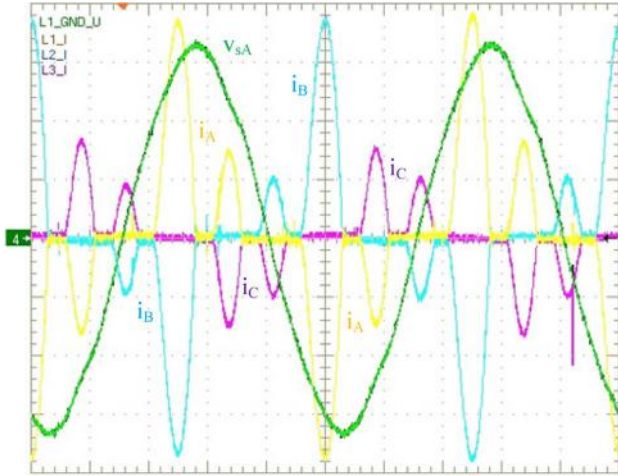
Fig. 20.   Mains input phase currents (20 A/div) and voltage (100 V/div) for pulsed operation.

6 ms when the LCC is set to deliver power to the load, and during the other 18 ms, the switches of the LCC converter are turned off.

In Fig. 19(a), the resonant tank current of the back-end converter (i_{Ls}), the output voltage V_{ESP}, the output current i_{ESP}, and the bus-bar capacitor voltage V_{in} are shown. Note that without pulse, the inverter switches are turned off, and no current flows through the circuit $(i_{Ls} = 0)$, and when the pulse is on, a high-frequency current is demanded. Fig. 19(b) shows the instant when the pulse is released, the resonant current i_{Ls}, the IGBTs full-bridge output voltage V_{AB}, and the transformer primary voltage V_{pri}. Importantly, during the pulse operation, a high-voltage drop in the DC-link voltage occurs, V_{in}; however, when the pulse control is off, the AC input currents can charge the bus-bar capacitor to voltages above the line-to-line voltages. As shown in Fig. 20, the oscillation in the bus-bar capacitor voltage causes high distortions in the line currents and also affect the LCC converter losses; thus, this effect should be considered in the LCC design. An active rectifier and/or an active power filter could be used to improve the line power quality and/or to keep the bus-bar voltage regulated [40].

VI. CONCLUSION

As seen in Fig. 18, the power module loss model is very accurate ($\pm 5\%$); this justifies its use in optimally designing the LCC resonant converter. One can also observe that for each commercial power module, there is a region where VF control would be preferable (full power operation) and another region where DC control gives better results (operation $< 70\% V_{o\_max}$). However, due to the high sparkover rate (output short-circuit rate), which can be around 10 to 50 times per second, and also the variation of dust concentration in the ESP bus sections, the power supplies operate for a considerable time in the region $< 70\% V_{o\_max}$, even when they are set to deliver full power. In this way, the most suitable control technique for this application is the DC control, but one has to accept the uneven distribution of losses among the bridge legs, which may occur.

APPENDIX

The LCC resonant converter large signal model for VF and DC controls is shown in the following.

VF and DC Controls		
Series resonant frequency	$f_0 = \dfrac{1}{2\pi\sqrt{L_s C_s}}$	(1)
Characteristic impedance	$Z_s = \sqrt{L_s/C_s}$	(2)
Normalized switching frequency	$f_{s,N} = \dfrac{f_s}{f_0}$	(3)
Ratio between the parallel and series capacitances	$\alpha = \dfrac{C_p}{C_s}$	(4)
Rectifier conduction angle	$\theta = 2\tan^{-1}\sqrt{\dfrac{\pi n^2 Z_s I_0}{2 f_{s,N}\alpha V_0}}$	(5)
Ratio of V_o and peak of the 1st harm. of the primary voltage	$k_v = 1 + 0.27\sin\left(\dfrac{\theta}{2}\right)$	(6)
Displacement of the fundamental voltage and current on the primary side	$\beta = -0.4363\sin(\theta)$	(7)
Dimensionless parameter	$\omega C_p R_e = \dfrac{\pi k_v^{\ 2}}{4\left(\tan\left(\frac{\theta}{2}\right)\right)^2}$	(8)
$k_{21} = \dfrac{1}{\sqrt{\left[1-\alpha(f_{s,N}^2-1)\left(1+\frac{\tan(|\beta|)}{\omega C_p R_e}\right)\right]^2 + \left[\frac{\alpha}{\omega C_p R_e}\left(f_{s,N}^2-1\right)\right]^2}}$		(9)
$\phi = \tan^{-1}\left(\dfrac{\alpha}{\omega C_p R_e}\left(f_{s,N}^2\left(1+\left[\omega C_p R_e+\tan(|\beta|)\right]^2\right)-1\right)\right.$ $\left. -\left[\omega C_p R_e+\tan(|\beta|)\right]\left[1+\alpha\left(1+\frac{\tan(|\beta|)}{\omega C_p R_e}\right)\right]\right)$		(10)

	VF Control	DC Control	
Duty cycle	D=1	$D = 1 - \dfrac{2}{\pi}\phi$	(11)
V_o function	$\dfrac{V_0}{nV_{in}} = \dfrac{4}{\pi}\dfrac{k_{21}}{k_v}\sin\left(D\dfrac{\pi}{2}\right)$		(12)
1st harm. peak of the I_{Ls}	$I_{Ls\,pk} = \dfrac{2f_{s,N}\alpha}{n(1+\cos(\theta))}\dfrac{V_0}{Z_s}$		(13)
1st harm. peak of the V_{Ls}	$V_{Ls\,pk} = I_{Ls\,pk}2\pi f_s L_s$		(14)
1st harm. peak of V_{Cs}	$U_{Cs\,pk} = \dfrac{I_{Ls\,pk}}{2\pi f_s C_s}$		(15)

	VF Control	DC Control	
Average (Avg) input current $I_{in\,avg}$	$\dfrac{2I_{Ls\,pk}}{\pi}\cos(\phi)$	$\dfrac{I_{Ls\,pk}}{\pi}(1-\cos(D\pi))$	(16)
ZVS leg turn-off current	$I_{Ls\,pk}\sin(\pi-\phi)$	$I_{Ls\,pk}\sin(D\pi)$	(17)
RMS current on the ZVS leg transistors $I_{C\ RMS}$	$\dfrac{\frac{I_{Ls\,pk}}{2}}{\sqrt{\frac{\pi-\phi}{\pi}-\frac{\sin(2(\pi-\phi))}{2\pi}}} *$	$\dfrac{I_{Ls\,pk}}{2}\sqrt{D-\dfrac{\sin(2D\pi)}{2\pi}}$	(18)

RMS current on the ZVS leg diodes $I_{D\ RMS}$	$\dfrac{I_{Ls\ pk}}{2} *$ $\sqrt{\dfrac{\phi}{\pi} + \dfrac{\sin(2(\pi - \phi))}{2\pi}}$	$\dfrac{I_{Ls\ pk}}{2} *$ $\sqrt{1 - D + \dfrac{\sin(2D\pi)}{2\pi}}$	(19)
Avg current on the ZVS leg transistors	$\dfrac{I_{Ls\ pk}}{\pi}(\cos(\frac{\phi}{2}))^2$	$\dfrac{I_{Ls\ pk}}{2\pi}(1 - \cos(D\pi))$	(20)
Avg current on the ZVS leg diodes	$\dfrac{I_{Ls\ pk}}{\pi}(\sin(\frac{\phi}{2}))^2$	$\dfrac{I_{Ls\ pk}}{2\pi}(1 + \cos(D\pi))$	(21)
ZCS leg RMS current	-	$I_{C\_RMS} = \dfrac{I_{Ls\ pk}}{2}$	(22)
ZCS leg Avg current	-	$I_{C\_avg} = \dfrac{I_{Ls\ pk}}{\pi}$	(23)
Transformer primary RMS current	$I_{T1\ rms} = I_0 \dfrac{n\sqrt[2]{2}}{k_v \cos\beta}$		(24)
Output diodes currents	$I_{D\ rms} = \dfrac{I_0}{k_v \cos\beta}$ and $I_{D\ avg} = \dfrac{I_0}{2}$		(25)
Conduct. loss	$P_{cond} = a_C \cdot I_C^2 + b_C \cdot I_C + c_C\ [W]$		(26)
Switching loss	$K_{IGBT} = a_S \cdot I_{C\_off}^2 + b_S \cdot I_{C\_off} + c_S\ [\frac{\mu Ws}{A}]$ $P_{Swt} = E \cdot f_S = K_{IGBT} \cdot I_{C\_off} \cdot f_S \cdot 10^{-6}[W]$		(27)
	$P_{T\_Cond} = \dfrac{1}{2\pi}[a_{TC}I_{Lspk}^2\left(\dfrac{\pi - \phi}{2} - \dfrac{\sin(2(\pi - \phi))}{4}\right)$ $+ 2b_{TC}I_{Lspk}(\cos(\frac{\phi}{2}))^2 + 2\pi c_{TC}]$		(28)
	$P_{D\_Cond} = \dfrac{1}{2\pi}[a_{DC}I_{Lspk}^2\left(\dfrac{\phi}{2} + \dfrac{\sin(2(\pi - \phi))}{4}\right)$ $+ 2b_{DC}I_{Lspk}(\sin(\frac{\phi}{2}))^2 + 2\pi c_{DC}]$		(29)
	$P_{T\_Swtch} = \dfrac{V_{in}I_{C\_off}f_S 10^{-6}}{u_S}[a_S I_{C\_off}^2 + b_S I_{C\_off} + c_S]$		(30)
	$P_{Total} = 4[P_{T\_Cond} + P_{D\_Cond} + P_{T\_Swtch}]$		(31)
	$P_{T\_ZVS\_Cond} = \dfrac{1}{2\pi}[a_{TC}I_{Lspk}^2\left(\dfrac{D\pi}{2} - \dfrac{\sin(2\pi D)}{4}\right) + b_{TC}I_{Lspk}(1$ $- \cos(D\pi)) + 2\pi c_{TC}]$		(32)
	$P_{D\_ZVS\_Cond} = \dfrac{1}{2\pi}[a_{DC}I_{Lspk}^2\left(\dfrac{(1 - D)\pi}{2} + \dfrac{\sin(2\pi D)}{4}\right)$ $+ b_{DC}I_{Lspk}(1 + \cos(D\pi)) + 2\pi c_{DC}]$		(33)
	$P_{T\_ZVS\_Swtch} = \dfrac{V_{in}I_{C\_off}f_S 10^{-6}}{u_S}[a_S I_{C\_off}^2 + b_S I_{C\_off} + c_S]$		(34)
	$P_{T\_ZCS\_Cond} = \dfrac{1}{2\pi}[\dfrac{\pi a_{TC}I_{Lspk}^2}{2} + 2b_{TC}I_{Lspk} + 2\pi c_{TC}]$		(35)
	$P_{T\_ZCS\_Swtch} = E_{optm}f_S$		(36)
	$P_{Total} = 2[P_{T\_ZVS\_Cond} + P_{D\_ZVS\_Cond} + P_{T\_ZVS\_Swtch} + P_{T\_ZCS\_Cond}$ $+ P_{T\_ZCS\_Swtch}]$		(37)
	$R_{th,S-A} = \dfrac{T_{Sink} - T_{Amb}}{P_{Total}}$		(38)

$P_{C,R} = V_{F,R}\dfrac{I_0}{2}$	(39)
$L_\sigma = \dfrac{N_2^2}{n^2}\dfrac{\mu_0(l_1 + l_2)}{h_1}\left(\dfrac{d_1 + d_2}{3} + d_0\right)$	(40)
$C_p = \dfrac{4e_e e_0 l_2 w(n_{layer} - 1)n^2}{3d n_{slot} n_{layer}^2}$	(41)
$P_d = \dfrac{1}{2}C U_{Cpp}^2 f_S \tan\delta$	(42)
$P_{tm} = R_c I_{Crms}^2$	(43)
$P_{LV} = \sum_{n=1}^{\infty} R_{DC,f}\dfrac{L_f}{\delta_{0,n}}[F_{f,n}i_{LV,n}^2 + G_{f,n}\dfrac{2(N_{LV}^2 - 1)}{3}i_{LV,n}^2]$	(44)
$R_{DC,f} = N_{LV}\dfrac{\rho_{cu}l_1}{L_f h_1}$	(45)
$P_{HV} = n_s \sum_{n=1}^{\infty} R_{DC,st}[F_{st,n}i_{HV,n}^2 + G_{st,n}\dfrac{i_{HV,n}^2}{8\pi^2 r_{bu}^2 n_s}$ $+ G_{st,n}F_{HV}^3\dfrac{n_{layer}(4n_{layer}^2 - 1)}{h_1^2}i_{HV,n}^2]$	(46)
$R_{DC,st} = N_{HV}\dfrac{4\rho_{cu}l_2}{\pi d_s^2}$	(47)
$penalty = \left(1 - \dfrac{V_{0act}}{V_{0ref}}\right)$	(48)

In (40) and (41), μ_0 is the absolute permeability; l_1 and l_2 are the average one turn lengths of the primary and the secondary windings; h_1, d_0, d_1, and d_2 are the geometric dimensions of the high-voltage transformer shown in Fig. 10; w is the height of one secondary windings; e_0 is the electric permittivity of vacuum; e_e is the equivalent relative permittivity of the oil-immersed paper; d is the distance between two layers of the secondary windings; n_{layer} is the number of layers of the secondary windings; and n_{slot} is the number of secondary windings.

In (42) and (43), C is the capacitance of the capacitor; U_{Cpp} is the peak-to-peak value of the ripple voltage across the capacitor; f_s is the operating frequency; $tan\delta$ is the dielectric loss factor; R_C is the series resistance of the used capacitor; and I_{Crms} is the rms current flowing through the capacitor. Note that $tan\delta$ and R_C can be derived from datasheets of the chosen capacitor.

In (44) and (45), ρ_{cu} is the resistivity of copper, $i_{LV,n}$ is the n-th harmonic component of the current, N_{LV} is the number of turns of the low voltage winding, L_f is the thickness of the foil, $\delta_{0,n}$ is the skin depth, $F_{f,n}$ is the skin effect factor for foils, and $G_{f,n}$ is the proximity effect factor for foils. The expressions for $\delta_{0,n}$, $F_{f,n}$, and $G_{f,n}$ can be found in [33].

In (46) and (47), $i_{HV,n}$ is the n-th harmonic component of the current, d_s is the diameter of one strand, n_s is the total amount of strands in the conductor, N_{HV} is the number of turns of the high-voltage winding, $F_{st,n}$ is the skin effect, and $G_{st,n}$ is the

proximity effect factor for a strand conductor. The expressions for $F_{st,n}$ and $G_{st,n}$ can be found in [33].

In (48), V_{0ref} is the output voltage specified point, and V_{0act} is the output voltage candidate point.

REFERENCES

[1] P. Ranstad, C. Mauritzson, M. Kirsten, and R. Ridgeway, "On experiences of the application of high-frequency power converters for ESP energization," in *Proc. ICESP*, 2004, pp. 1–16.

[2] T. Soeiro, J. Biela, J. Muhlethaler, J. Linner, P. Ranstad, and J. W. Kolar, "Optimal design of resonant converter for electrostatic precipitators," in *Proc. IPEC*, Sapporo, Japan, Jun. 2010, pp. 2294–2301.

[3] N. Grass and W. Hartmann, "Application of different types of high-voltage supplies on industrial ESP," *IEEE Tran. Ind. Appl.*, vol. 40, no. 6, pp. 1513–1520, Nov./Dec. 2004.

[4] T. Soeiro, J. Biela, J. Linner, P. Ranstad, and J. W. Kolar, "Line power quality improvement for pulsed electrostatic precipitator systems," in *Proc. IPEC*, Sapporo, Japan, Jun. 2010, pp. 1512–1519.

[5] T. Soeiro, J. Biela, J. Linner, P. Ranstad, and W. K. Johann, "Comparison of concepts for improving the line power quality of electrostatic precipitator systems," in *Proc. IEEE IECON*, Phoenix, AZ, Nov. 2010, pp. 1969–1974.

[6] P. Ranstad and H.-P. Nee, "On the distribution of AC and DC winding capacitances in high-frequency power transformer with rectifier loads," *IEEE Trans. Ind. Electron.*, vol. 58, no. 5, pp. 1789–1798, May 2011.

[7] D. Fu, F. C. Lee, Y. Qiu, and F. Wang, "A novel high-power-density three level LCC resonant converter with constant-power-factor-control for charging applications," *IEEE Trans. Power Electron.*, vol. 23, no. 5, pp. 2411–2420, May 2008.

[8] P. Karlsson, M. Bojrup, M. Alakula, and L. Gertmar, "Zero voltage switching converters," in *Proc. NORPIE*, Aalborg, Denmark, Jun. 2000, pp. 84–88.

[9] Z. Pantic, S. Bai, and S. M. Lukic, "ZCS LCC-compensated resonant inverter for inductive-power-transfer application," *IEEE Trans. Ind. Electron.*, vol. 58, no. 8, pp. 3500–3510, Aug. 2011.

[10] R. L. Steigerwald, "A comparison of half-bridge resonant converter topologies," *IEEE Trans. Power Electron.*, vol. 3, no. 2, pp. 174–182, Apr. 1988.

[11] P. Ranstad, "Design and control aspects on components and systems in high-voltage converters for industrial applications," M.S. thesis, Royal Inst. Technol., Stockholm, Sweden, 2010.

[12] J. Liu, L. Sheng, J. Shi, Z. Zhang, and X. He, "LCC resonant converter operating under discontinuous resonant current mode in high voltage high power and high frequency applications," in *Proc. APEC*, 2009, pp. 1482–1486.

[13] B.-R. Lin and S.-F. Wu, "ZVS resonant converter with series-connected transformers," *IEEE Trans. Ind. Electron.*, vol. 58, no. 8, pp. 3547–3554, Aug. 2011.

[14] B.-R. Lin and J.-Y. Dong, "ZVS resonant converter with parallel-series transformer connection," *IEEE Trans. Ind. Electron.*, vol. 58, no. 7, pp. 2972–2979, Jul. 2011.

[15] S. Chen, Z. Li, and C. Chen, "Analysis and design of single-stage AC/DC LLC resonant converter," *IEEE Trans. Ind. Electron.*, vol. 59, no. 3, pp. 1538–1544, Mar. 2012.

[16] T. Melaa, A. K. Ådnanes, K. Öye, T. F. Nestli, R. Nilsen, and P. Ranstad, "Evaluation of resonant converters for increased soft switching range," in *Proc. Conf. EPE*, 1997, pp. 4.419–4.425.

[17] F. S. Cavalcante and J. W. Kolar, "Design of a 5 kW high output voltage series-parallel resonant converter," in *Proc. IEEE Power Elect. Spec. Conf.*, 2003, vol. 4, pp. 1807–1814.

[18] N. Grass, "Fuzzy logic-optimising IGBT inverter for electrostatic precipitators," in *Conf. Rec. IEEE IAS Annu. Meeting*, Oct. 1999, vol. 4, pp. 2457–2462.

[19] B.-R. Lin, J.-Y. Dong, and J.-J. Chen, "Analysis and implementation of a ZVS/ZCS DC-DC switching converter with voltage step-up," *IEEE Trans. Ind. Electron.*, vol. 58, no. 7, pp. 2962–2971, Jul. 2011.

[20] G. Ivensky, A. Kats, and S. Ben-Yaakov, "A novel rc model of capacitive-loaded parallel and series-parallel resonant DC-DC converters," in *Proc. IEEE PESC*, 1997, pp. 958–964.

[21] A. K. S. Bhat, "A resonant converter suitable for 650 V dc bus operation," *IEEE Tran. Power Elect.*, vol. 6, no. 4, pp. 739–748, Oct. 1991.

[22] R. Beiranvand, R. Rashidian, M. R. Zolghadri, and S. M. Alavi, "Using LLC resonant converter for designing wide-range voltage source," *IEEE Trans. Ind. Electron.*, vol. 58, no. 5, pp. 1746–1756, May 2011.

[23] X. Wu, G. Hua, J. Zhang, and Z. Qian, "A new current-driven synchronous rectifier for series-parallel resonant (LLC) DC-DC converter," *IEEE Trans. Ind. Electron.*, vol. 58, no. 1, pp. 289–297, Jan. 2011.

[24] D. E. Goldberg, *Genetic Algorithms in Search, Optimization and Machine Learning*. New York: Addison-Wesley, 1989.

[25] P. Ranstad, H. P. Nee, and J. Linner, "A novel control strategy applied to the series loaded resonant converter," in *Proc. Conf. EPE*, Dresden, Germany, 2005, pp. 1–10.

[26] U. Drofenik and J. W. Kolar, "A general scheme for calculating switching-and conduction-losses of power semiconductors in numerical circuit simulations of power electronic systems," in *Proc. IPEC*, Niigata, Japan, 2005.

[27] J. C. Fothergill, P. W. Devine, and P. W. Lefley, "A novel prototype design for a transformer for high voltage, high frequency, high power use," *IEEE Trans. Power Del.*, vol. 16, no. 1, pp. 89–98, Jan. 2001.

[28] Y. Wang, Y. Huang, D. Xiao, and S. Qin, "Insulation structure analysis of high-frequency and high-voltage rectifier transformer," in *Proc. Int. Conf. Properties Appl. Dielect. Mater.*, Jul. 2009, pp. 154–157.

[29] W. T. McLyman, *Transformer and Inductor Design Handbook*. New York: Marcel Dekker, 2004.

[30] J. Biela and J. W. Kolar, "Using transformer parasitics for resonant converters—A review of the calculation of the stray capacitance of transformers," in *Conf. Rec. IEEE IAS Annu. Meeting*, 2005, pp. 1868–1875.

[31] K. Venkatachalam, T. Abdallah, and H. Tacca, "Accurate prediction of ferrite core loss with nonsinusoidal waveforms using only steinmetz parameters," in *Proc. IEEE Workshop Comput. Power Electron.*, Jun. 3–4, 2002, pp. 36–41.

[32] W. G. Hurley, E. Gath, and J. G. Breslin, "Optimizing the AC resistance of multilayer transformer windings with arbitrary current waveforms," *IEEE Trans. Power Elect.*, vol. 15, no. 2, pp. 369–376, Mar. 2000.

[33] P. Dowell, "Effects of eddy currents in transformer windings," *Proc. Inst. Elect. Eng.*, vol. 113, no. 8, pp. 1387–1394, Aug. 1966.

[34] I. Villar, U. Vicarret, I. Etxeberria-Otadui, and A. Rufer, "Global loss evaluation methods for nonsinusoidally fed medium-frequency power transformer," *IEEE Trans. Ind. Electron.*, vol. 56, no. 10, pp. 4132–4140, Oct. 2009.

[35] P. Ranstad and H.-P. Nee, "On dynamic effects influencing IGBT losses in soft-switching converters," *IEEE Trans. Power Elect.*, vol. 26, no. 1, pp. 260–271, Jan. 2011.

[36] J. Michael and Y. Rahmat, "Genetic algorithms in engineering electromagnetics," *IEEE Antennas Propag. Mag.*, vol. 39, no. 4, pp. 7–21, Aug. 1997.

[37] J. A. Vasconcelos, J. A. Ramirez, R. H. C. Takahashi, and R. R. Saldanha, "Improvements in genetic algorithms," *IEEE Trans. Magn.*, vol. 37, no. 5, pp. 3414–3417, Sep. 2001.

[38] K. F. Man, K. S. Tang, and S. Kwong, "Genetic algorithms: Concepts and applications," *IEEE Trans. Ind. Electron.*, vol. 43, no. 5, pp. 519–534, Oct. 1996.

[39] J. L. Ribeiro, P. C. Treleaven, and C. Alippi, "Genetic-algorithm programming environments," *Computer*, vol. 27, no. 6, pp. 28–43, Jun. 1994.

[40] T. B. Soeiro, T. Friedli, J. Linner, P. Ranstad, and J. W. Kolar, "Comparison of eletrostatic precipitator power supplies with low effects on the mains," in *Proc. ECCE Asia*, Jeju, Korea, May 2011, pp. 2382–2389.

Thiago B. Soeiro received the B.S. (with honors) and M.S. degrees in electrical engineering from the Federal University of Santa Catarina, Florianopolis, Brazil, in 2004 and 2007, respectively, and the Ph.D. degree from the Swiss Federal Institute of Technology (ETH Zurich), Zurich, Switzerland, in 2012.

He received the Best Paper 1st Prize Award at the IEEE ECCE Asia 2011. His research interests include power supplies for electrostatic precipitators and power factor correction techniques.

Jonas Mühlethaler received the M.Sc. and Ph.D. degrees in electrical engineering from the Swiss Federal Institute of Technology Zurich (ETHZ), Switzerland, in 2008 and 2012, respectively. During his Master's studies, he focused on power electronics and electrical machines. In his M.Sc. thesis, which he wrote at ABB Corporate Research in Sweden, he worked on compensating torque pulsation in permanent-magnet motors.

In 2008, he joined the Power Electronic Systems Laboratory (PES), ETHZ, to work toward the Ph.D. degree. During his Ph.D. studies, he worked on modeling and multi-objective optimization of inductive power components. Currently, he is a Postdoctoral Fellow in the PES.

Jörgen Linnér was born in Växjö, Sweden, 1974. He received the B.S. degree in electrical engineering from Växjö Universitet, Växjö, Sweden, in 1997.

He started at Alstom, Växjö, in 1997 working with field service and start-up activities, customer support, and application design support for the AQCS Product Line. In 2002, he joined the R&D power electronics group. Currently, he is acting as an R&D Project Leader within the Alstom Power Thermal Service AQCS Product Line R&D Center in Växjö. He is a coauthor of several publications and patents.

Per Ranstad (M'03) was born in Högby, Sweden, in 1958. He received the M.Sc. degree in electrical engineering from Lunds Institute of Technology, Lund, Sweden, in 1987, and the Licenciate and Ph.D. degrees in electrical engineering from the Royal Institute of Technology, Stockholm, Sweden, in 2004 and 2010, respectively.

He is a Senior Researcher with Alstom Power, Växjö, Sweden, and has been heading R&D activities in the area of power converters for industrial applications for more than 20 years. His main research interests are high-voltage transformers, power semiconductors, resonant topologies, and converter control.

Dr. Ranstad was awarded the Masuda Award by the International Society for Electrostatic Precipitation at the 12th International Conference on Electrostatic Precipitation in Nuremberg, Germany, in May 2011.

Johann W. Kolar (F'10) received the M.Sc. and Ph.D. degrees (*summa cum laude/promotio sub auspiciis praesidentis rei publicae*) from the University of Technology Vienna, Austria.

Since 1984, he has been working as an independent international consultant in close collaboration with the University of Technology Vienna, in the fields of power electronics, industrial electronics, and high-performance drives. He has proposed numerous novel converter topologies and modulation/control concepts, e.g., the VIENNA Rectifier, the Swiss Rectifier, and the three-phase AC-AC Sparse Matrix Converter. He has published over 450 scientific papers in international journals and conference proceedings and has filed more than 85 patents. He was appointed Professor and Head of the Power Electronic Systems Laboratory at the Swiss Federal Institute of Technology (ETH) Zurich, Switzerland, on February 1, 2001. The focus of his current research is on AC–AC and AC–DC converter topologies with low effects on the mains, e.g., for data centers, more-electric-aircraft and distributed renewable energy systems, and on solid-state transformers for smart microgrid systems. Further main research areas are the realization of ultra-compact and ultra-efficient converter modules employing latest power semiconductor technology (SiC and GaN), micro power electronics and/or power supplies on chip, multi-domain/scale modeling/simulation and multi-objective optimization, physical model-based lifetime prediction, pulsed power, and ultra-high speed and bearingless motors.

Prof. Kolar received the Best TRANSACTIONS Paper Award of the IEEE Industrial Electronics Society in 2005, the Best Paper Award of the ICPE in 2007, the 1st Prize Paper Award of the IEEE IAS IPCC in 2008, the IEEE IECON Best Paper Award of the IES PETC in 2009, the IEEE PELS TRANSACTIONS Prize Paper Award 2009, the Best Paper Award of the IEEE/ASME TRANSACTIONS ON MECHATRONICS 2010, the IEEE PELS TRANSACTIONS Prize Paper Award 2010, the Best Paper 1st Prize Award at the IEEE ECCE Asia 2011, the 1st Place IEEE IAS Society Prize Paper Award 2011 and the IEEE IAS EMC Paper Award 2012. Furthermore, he received the ETH Zurich Golden Owl Award 2011 for Excellence in Teaching. He also received an Erskine Fellowship from the University of Canterbury, New Zealand, in 2003. He initiated and/or is the founder/cofounder of four spin-off companies targeting ultra-high speed drives, multi-domain/level simulation, ultra-compact/efficient converter systems, and pulsed power/electronic energy processing. In 2006, the European Power Supplies Manufacturers Association awarded the Power Electronics Systems Laboratory of ETH Zurich as the leading academic research institution in Power Electronics in Europe. He is a Member of the IEEJ and of International Steering Committees and Technical Program Committees of numerous international conferences in the field (e.g., Director of the Power Quality Branch of the International Conference on Power Conversion and Intelligent Motion). He is the founding Chairman of the IEEE PELS Austria and Switzerland Chapter and Chairman of the Education Chapter of the EPE Association. From 1997 through 2000, he served as an Associate Editor of the IEEE TRANSACTIONS ON INDUSTRIAL ELECTRONICS and since 2001 he has been serving as an Associate Editor of the IEEE TRANSACTIONS ON POWER ELECTRONICS. Since 2002, he has also been an Associate Editor of the *Journal of Power Electronics* of the Korean Institute of Power Electronics and a Member of the Editorial Advisory Board of the *IEEJ Transactions on Electrical and Electronic Engineering*. He was appointed an IEEE Distinguished Lecturer by the IEEE Power Electronics Society in 2011.